

Variational Mapping of Chern Bands to Landau Levels: Application to Fractional Chern Insulators in Twisted MoTe₂

Bohao Li¹ and Fengcheng Wu^{1,2,*}

¹*School of Physics and Technology, Wuhan University, Wuhan 430072, China*

²*Wuhan Institute of Quantum Technology, Wuhan 430206, China*

We present a theoretical study of mapping between Chern bands and generalized Landau levels in twisted bilayer MoTe₂ (*t*MoTe₂), where fractional Chern insulators down to zero magnetic fields have been observed. We construct an exact Landau-level representation of moiré bands, where the basis functions, characterized by a uniform quantum geometry, are derived from Landau-level wavefunctions dressed by spinors aligned or antialigned with the layer pseudospin skyrmion field. We further generalize the dressed zeroth Landau level to a variational wavefunction with an ideal yet nonuniform quantum geometry and variationally maximize its weight in the first moiré band. The variational wavefunction has a high overlap with the first band and quantitatively captures the exact diagonalization spectra of fractional Chern insulators at hole-filling factors $\nu_h = 2/3$ and $3/5$, providing a clear theoretical mechanism for the formation and properties of the fractionalized states. Our work introduces a variational approach to studying fractional states by mapping Chern bands to Landau levels, with application to other systems beyond *t*MoTe₂ also demonstrated.

I. INTRODUCTION

Fractional Chern insulators (FCIs), proposed in theory [1–5] as lattice generalizations of fractional quantum Hall states in Landau levels (LLs), have now been observed in several van der Waals heterostructures [6–12]. Among them, FCIs at zero magnetic field, also known as fractional quantum anomalous Hall insulators, were first realized in *t*MoTe₂ [8–11]. Transport studies of *t*MoTe₂ have identified both integer Chern insulators at $\nu_h = 1$ and FCIs at $\nu_h = 2/3$ and $3/5$ [10, 11], further characterized through the optical spectrum [8, 9], electronic compressibility [9] and real-space local imaging [13, 14]. In addition, a recent experiment has reported evidence of fractional quantum spin Hall effect in *t*MoTe₂ at $\nu_h = 3$ [15]. While earlier theoretical studies predicted Chern bands [16–18] and FCIs [19–21] in twisted transition metal dichalcogenide homobilayers, the experimental breakthroughs have sparked many further theoretical investigations into the rich quantum phases of matter in this system [22–52].

The microscopic mechanism underlying the formation of FCIs is a fundamental theoretical question. One approach involves establishing connections between Bloch Chern bands and LLs [53–69]. In *t*MoTe₂, the first moiré valence band has a Chern number $|C| = 1$ and nearly, though not exactly, saturates the trace inequality for quantum geometry at a magic twist angle θ_m , signaling similarities with the zeroth LL (0LL) [23]. Remarkably, the exact-diagonalization (ED) spectra of *t*MoTe₂, with the many-body Hamiltonian projected onto the first band, resembles those of 0LL, aiding in the numerical determination of FCIs at ν_h with odd denominators and composite Fermi liquid at $\nu_h = 1/2$ [22–25]. Connections between topological moiré bands in *t*MoTe₂ and LLs have

been made in different approximate limits [39–41], but a quantitative mapping strategy in the generic case is still lacking.

Here we introduce a strategy that begins with an exact LL representation of moiré bands in *t*MoTe₂. The construction is motivated by the layer pseudospin field, which forms a skyrmion lattice [16] and generates a non-Abelian gauge field in the local frame [17, 39]. The Bloch bases in this representation consist of *dressed* LL wavefunctions [Eq. (10)] that maintain uniform quantum geometry. The average weight of the first moiré band on the dressed 0LL states is considerable (~ 0.75) but noticeably below unity at θ_m . We then extend the dressed 0LL states to generalized 0LL wavefunctions [Eq. (12)] with an ideal (i.e., saturated trace inequality) but nonuniform quantum geometry [61] and optimize their weight in the first moiré band using a variational approach, reaching a maximum of 0.95 at θ_m . The generalized 0LL wavefunctions capture the density fluctuation in the Chern band and host exact FCI ground state for certain short-range interactions. The obtained high weight provides an intuitive explanation of the emergence of FCIs in *t*MoTe₂. We also perform ED studies with Coulomb interactions projected onto both the original wavefunction of the first band and the variational wavefunction. Both models consistently yield FCIs at $\nu_h = 2/3$ and $3/5$, with a quantitative agreement in the energy spectra. Based on the variational wavefunction, we quantitatively examine the effect of density fluctuation on FCIs, explaining their twist angle dependence. We further demonstrate the mapping in a model system [70] beyond *t*MoTe₂, showing the generic applicability of our approach. This mapping strategy enables the application of physics from fractional quantum Hall states to FCIs and the design of new systems that host FCIs.

This paper is organized as follows. In Sec. II, we present the single-particle Hamiltonian and band structure of *t*MoTe₂. In Sec. III, we construct the dressed LL bases for the first moiré Chern band. Section IV develops

* wufcheng@whu.edu.cn

the variational approach for mapping the Chern band to the generalized 0LL. In Sec. V, we perform ED studies of FCIs, using both the original and variational wavefunctions. Section VI explores further applications in a model system without the emergent magnetic field. Finally, we conclude with a discussion in Sec. VII. Technical details are provided in Appendices A and B.

II. MOIRÉ HAMILTONIAN

Moiré Hamiltonian for valence states in $t\text{MoTe}_2$ at $+K$ valley is given by [16, 30],

$$H = \begin{pmatrix} -\frac{\hbar^2(\hat{\mathbf{k}}-\boldsymbol{\kappa}_+)^2}{2m^*} + \Delta_+(\mathbf{r}) & \Delta_t(\mathbf{r}) \\ \Delta_t^\dagger(\mathbf{r}) & -\frac{\hbar^2(\hat{\mathbf{k}}-\boldsymbol{\kappa}_-)^2}{2m^*} + \Delta_-(\mathbf{r}) \end{pmatrix}, \quad (1)$$

where $\hat{\mathbf{k}}$ is the momentum operator, m^* is the effective mass, $\boldsymbol{\kappa}_\pm = \frac{4\pi}{3a_M}(-\frac{\sqrt{3}}{2}, \mp\frac{1}{2})$ are located at corners of moiré Brillouin zone, $a_M \approx a_0/\theta$ is the moiré period, θ is the twist angle, and $a_0 = 3.52 \text{ \AA}$ is the monolayer lattice constant. $\Delta_\pm(\mathbf{r})$ and $\Delta_t(\mathbf{r})$ are given by

$$\begin{aligned} \Delta_\pm(\mathbf{r}) &= 2V_1 \sum_{j=1,3,5} \cos(\mathbf{g}_j^{(1)} \cdot \mathbf{r} \pm \psi) + 2V_2 \sum_{j=1,3,5} \cos(\mathbf{g}_j^{(2)} \cdot \mathbf{r}), \\ \Delta_t(\mathbf{r}) &= w_1(1 + e^{-i\mathbf{g}_2^{(1)} \cdot \mathbf{r}} + e^{-i\mathbf{g}_3^{(1)} \cdot \mathbf{r}}) \\ &\quad + w_2(e^{-i\mathbf{g}_2^{(2)} \cdot \mathbf{r}} + e^{-i\mathbf{g}_1^{(1)} \cdot \mathbf{r}} + e^{-i\mathbf{g}_4^{(1)} \cdot \mathbf{r}}), \end{aligned} \quad (2)$$

where $\mathbf{g}_i^{(1)} = \frac{4\pi}{\sqrt{3}a_M}[\cos \frac{\pi(i-1)}{3}, \sin \frac{\pi(i-1)}{3}]$ and $\mathbf{g}_i^{(2)} = \frac{4\pi}{a_M}[\cos \frac{\pi(2i-1)}{6}, \sin \frac{\pi(2i-1)}{6}]$ are moiré reciprocal lattice vectors. We use model parameters fitted from first-principles band structure at $\theta = 3.89^\circ$ [30], where the effective mass $m^* = 0.62 m_e$ (m_e is the electron rest mass) and $(\psi, V_1, w_1, V_2, w_2) = (-88.43^\circ, 7.94 \text{ meV}, -10.77 \text{ meV}, 20.00 \text{ meV}, 10.21 \text{ meV})$. Here we use this particular set of parameters to illustrate the main physics [25–30].

A representative moiré band structure is shown in Fig. 1(a). We focus on the first moiré valence band with a narrow bandwidth and a Chern number $\mathcal{C} = +1$. The quantum geometry of this band, as characterized by Berry curvature $\Omega_{\mathbf{k}}$ and trace of quantum metric $\text{Tr } g_{\mathbf{k}}$, is illustrated in Fig. 2 for $\theta = 2.9^\circ$. Here $\Omega_{\mathbf{k}}$ is positive definite and fluctuates in sync with $\text{Tr } g_{\mathbf{k}}$. A measure of the deviation from ideal quantum geometry [59, 61] is $T = \frac{1}{2\pi} \int d^2\mathbf{k} \text{Tr } g_{\mathbf{k}} - |\mathcal{C}|$, which is bounded by $T \geq 0$ (i.e., the trace inequality). The θ dependence of T is plotted in Fig. 1(b), which is minimum ($T \sim 0.1$) at the magic angle $\theta_m = 2.9^\circ$. The small value of T at θ_m implies a connection with the generalized 0LL, which has a nonuniform but ideal quantum geometry (i.e., $T = 0$).

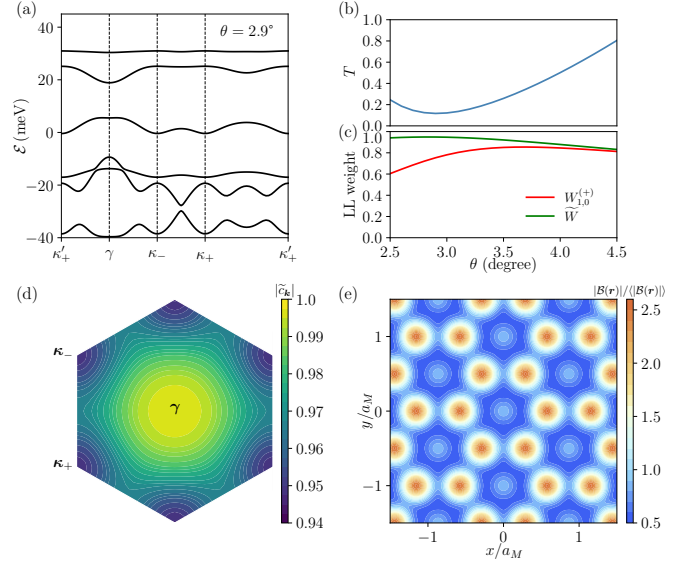


FIG. 1. (a) Moiré band structure of $t\text{MoTe}_2$ at $\theta = 2.9^\circ$. (b) T of the first band as a function of θ . (c) LL weight $W_{1,0}^{(+)}$ (red line) and \tilde{W} (green line) as functions of θ . (d) Overlap $|\tilde{c}_{\mathbf{k}}| = |\langle \varphi_{1,\mathbf{k}} | \Theta_{\mathbf{k}} \rangle|$ in moiré Brillouin zone. (e) Map of $|\mathcal{B}(\mathbf{r})|$ scaled by its spatial average. θ is 2.9° in (d) and (e).

III. LANDAU LEVEL REPRESENTATION

We apply two unitary transformations to H to find a representation of Bloch states in terms of LL wavefunctions. The first unitary transformation is to recast the Hamiltonian into the form of a particle moving in a scalar potential $\Delta_0(\mathbf{r})$ and a layer pseudospin field $\boldsymbol{\Delta}(\mathbf{r})$ that forms a skyrmion lattice,

$$\begin{aligned} H_1 &= U_0^\dagger(\mathbf{r}) H U_0(\mathbf{r}), \\ &= -\frac{\hbar^2 \hat{\mathbf{k}}^2}{2m^*} \sigma_0 + \boldsymbol{\Delta}(\mathbf{r}) \cdot \boldsymbol{\sigma} + \Delta_0(\mathbf{r}) \sigma_0, \end{aligned} \quad (3)$$

where $U_0(\mathbf{r}) = \text{diag}(e^{i\boldsymbol{\kappa}_+ \cdot \mathbf{r}}, e^{i\boldsymbol{\kappa}_- \cdot \mathbf{r}})$, σ_0 is the identity matrix and $\boldsymbol{\sigma}$ are Pauli matrices. The skyrmion field $\boldsymbol{\Delta}(\mathbf{r})$ has a nontrivial winding number,

$$N_w = \frac{1}{2\pi} \int_{\mathcal{A}_0} d\mathbf{r} b_z = -1. \quad (4)$$

Here \mathcal{A}_0 is the area expanded by a moiré unit cell, $b_z = \frac{1}{2} \mathbf{n} \cdot (\partial_x \mathbf{n} \times \partial_y \mathbf{n})$, and $\mathbf{n}(\mathbf{r}) = \boldsymbol{\Delta}(\mathbf{r})/|\boldsymbol{\Delta}(\mathbf{r})|$. An illustration of the skyrmion lattice formed by the unit vector $\mathbf{n}(\mathbf{r})$ is shown in Fig. 3(a).

The skyrmion field generates an emergent magnetic field in the adiabatic limit [71], which facilitates the mapping to LLs. We construct another unitary matrix $U(\mathbf{r})$ to rotate the layer pseudospin to the local frame of $\boldsymbol{\Delta}(\mathbf{r})$,

$$\begin{aligned} U^\dagger(\mathbf{r}) [\boldsymbol{\Delta}(\mathbf{r}) \cdot \boldsymbol{\sigma}] U(\mathbf{r}) &= |\boldsymbol{\Delta}(\mathbf{r})| \sigma_z, \\ U(\mathbf{r}) &= (\chi^{(+)}(\mathbf{r}), \chi^{(-)}(\mathbf{r})), \end{aligned} \quad (5)$$

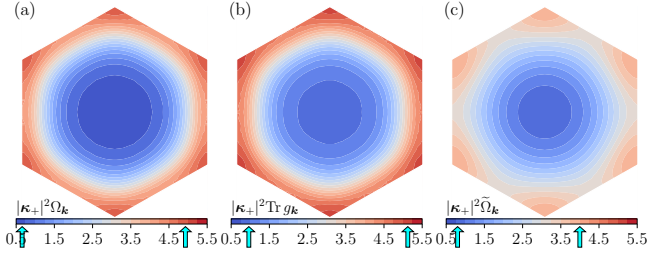


FIG. 2. (a) $\Omega_{\mathbf{k}}$ and (b) $\text{Tr } g_{\mathbf{k}}$ for $\varphi_{1,\mathbf{k}}(\mathbf{r})$ in the moiré Brillouin zone. (c) $\tilde{\Omega}_{\mathbf{k}}$ (identical to $\text{Tr } \tilde{g}_{\mathbf{k}}$) for $\Theta_{\mathbf{k}}(\mathbf{r})$. The arrows indicate the data range in each plot. θ is 2.9° .

where $\chi^{(+)}$ and $\chi^{(-)}$ are spinors that align and antialign with Δ , respectively. The nonzero winding number N_w poses an obstruction in choosing the phases of $\chi^{(\pm)}$ such that $U(\mathbf{r})$ is spatially continuous and periodic. However, $U(\mathbf{r})$ can be continuous but quasiperiodic. This motivates us to express $U(\mathbf{r})$ using LL wavefunctions,

$$\begin{aligned}\chi^{(+)}(\mathbf{r}) &= \{\alpha(\mathbf{r})\Psi_{0,\kappa_-}^{(+)}(\mathbf{r}), \beta(\mathbf{r})\Psi_{0,\kappa_+}^{(+)}(\mathbf{r})\}^T, \\ \chi^{(-)}(\mathbf{r}) &= \{\beta^*(\mathbf{r})[\Psi_{0,\kappa_+}^{(+)}(\mathbf{r})]^*, -\alpha^*(\mathbf{r})[\Psi_{0,\kappa_-}^{(+)}(\mathbf{r})]^*\}^T.\end{aligned}\quad (6)$$

Here $\Psi_{n,\mathbf{k}}^{(\pm)}(\mathbf{r})$ denotes electron magnetic Bloch wavefunction of the n th LL at momentum \mathbf{k} in magnetic field along $\pm \hat{z}$ direction. The expression of the 0LL wavefunction $\Psi_{0,\mathbf{k}}^{(+)}(\mathbf{r})$ employed in Eq. (6) is provided in Appendix A.

One solution of functions $\alpha(\mathbf{r})$ and $\beta(\mathbf{r})$ in Eq. (6) is,

$$\begin{aligned}\alpha(\mathbf{r}) &= e^{-i\zeta(\mathbf{r})/2} \sqrt{[1 + n_z(\mathbf{r})]/2} |\Psi_{0,\kappa_-}^{(+)}(\mathbf{r})|, \\ \beta(\mathbf{r}) &= e^{i\zeta(\mathbf{r})/2} \sqrt{[1 - n_z(\mathbf{r})]/2} |\Psi_{0,\kappa_+}^{(+)}(\mathbf{r})|, \\ \zeta(\mathbf{r}) &= \text{Arg}\{[n_x(\mathbf{r}) + in_y(\mathbf{r})]/[\Psi_{0,\kappa_-}^{(+)}(\mathbf{r})]^* \Psi_{0,\kappa_+}^{(+)}(\mathbf{r})\}.\end{aligned}\quad (7)$$

Here $n_{x,y,z}$ are components of \mathbf{n} . Because the zeros of $|\Psi_{0,\kappa_\mp}^{(+)}(\mathbf{r})|$ and $[\Psi_{0,\kappa_-}^{(+)}(\mathbf{r})]^* \Psi_{0,\kappa_+}^{(+)}(\mathbf{r})$ are exactly canceled, respectively, by those of $\sqrt{1 \pm n_z(\mathbf{r})}$ and $n_x(\mathbf{r}) + in_y(\mathbf{r})$, $\alpha(\mathbf{r})$ and $\beta(\mathbf{r})$ are periodic functions without singularity. Therefore, the spinors $\chi^{(\pm)}(\mathbf{r})$ obey *magnetic* Bloch's theorem under lattice translation, making $U(\mathbf{r})$ quasiperiodic. The point group symmetry of $U(\mathbf{r})$ is analyzed in Appendix A.

We now apply $U(\mathbf{r})$ to the Hamiltonian H_1 ,

$$\begin{aligned}H_2 &= U^\dagger(\mathbf{r})H_1U(\mathbf{r}) \\ &= -\frac{\hbar^2}{2m^*} \begin{pmatrix} (\hat{\mathbf{k}} + \mathbf{A}_{11})^2 & \hat{\mathbf{k}}\mathbf{A}_{12} + \mathbf{A}_{12}\hat{\mathbf{k}} \\ \hat{\mathbf{k}}\mathbf{A}_{21} + \mathbf{A}_{21}\hat{\mathbf{k}} & (\hat{\mathbf{k}} + \mathbf{A}_{22})^2 \end{pmatrix} \\ &\quad + |\Delta(\mathbf{r})|\sigma_z + [\Delta_0(\mathbf{r}) - D(\mathbf{r})]\sigma_0,\end{aligned}\quad (8)$$

where $\mathbf{A} = -iU^\dagger(\mathbf{r})\nabla U(\mathbf{r})$ is a non-Abelian gauge field generated by the skyrmion field and $D(\mathbf{r}) = \frac{\hbar^2}{2m^*}|\mathbf{A}_{12}|^2$ [17, 39]. The field \mathbf{A}_{ii} generates an effective magnetic field $B_i = (\hbar/e)\nabla \times \mathbf{A}_{ii}$ with $B_1 = +(\hbar/e)b_z$ and

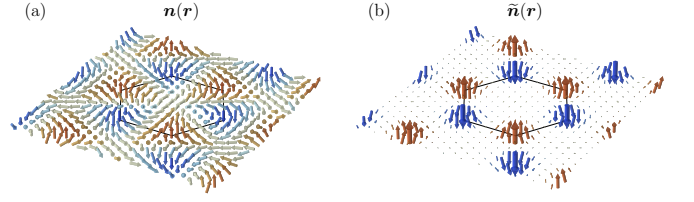


FIG. 3. (a), (b) Plot of $\mathbf{n}(\mathbf{r})$ and $\tilde{\mathbf{n}}(\mathbf{r})$, with color encoding the \hat{z} component. The hexagon marks the Wigner-Seitz cell.

$B_2 = -(\hbar/e)b_z$. The flux of B_1 (B_2) over \mathcal{A}_0 is exactly a negative (positive) magnetic flux quantum, according to Eq. (4). Therefore, wavefunction $\Phi_{m,\mathbf{k}}(\mathbf{r})$ of Hamiltonian H_2 for the m th band at momentum \mathbf{k} can be expanded using the magnetic Bloch state $\Psi_{n,\mathbf{k}}^{(\pm)}(\mathbf{r})$,

$$\Phi_{m,\mathbf{k}}(\mathbf{r}) = \sum_n [c_{m,n,\mathbf{k}}^{(+)} \Psi_{n,\mathbf{k}}^{(-)}(\mathbf{r}), c_{m,n,\mathbf{k}}^{(-)} \Psi_{n,\mathbf{k}}^{(+)}(\mathbf{r})]^T, \quad (9)$$

where $c_{m,n,\mathbf{k}}^{(\pm)}$ are expansion coefficients.

The Bloch state $\varphi_{m,\mathbf{k}}(\mathbf{r})$ of the original Hamiltonian H is related to $\Phi_{m,\mathbf{k}}(\mathbf{r})$ by unitary transformations,

$$\begin{aligned}\varphi_{m,\mathbf{k}}(\mathbf{r}) &= U_0(\mathbf{r})U(\mathbf{r})\Phi_{m,\mathbf{k}}(\mathbf{r}) \\ &= \sum_n \sum_{s=\pm} c_{m,n,\mathbf{k}}^{(s)} \psi_{n,\mathbf{k}}^{(s)}(\mathbf{r}).\end{aligned}\quad (10)$$

Here $\psi_{n,\mathbf{k}}^{(s)}(\mathbf{r}) = U_0(\mathbf{r})\chi^{(s)}\Psi_{n,\mathbf{k}}^{(-s)}$ are a set of orthonormal and complete Bloch bases, which can be understood as the LL wavefunction $\Psi_{n,\mathbf{k}}^{(-s)}$ dressed by the spinor $U_0(\mathbf{r})\chi^{(s)}$. Because $\chi^{(s)}$ and $\Psi_{n,\mathbf{k}}^{(-s)}$ are magnetic Bloch states under opposite magnetic fields, $\psi_{n,\mathbf{k}}^{(\pm)}$ satisfy Bloch's theorem. Notably, $\psi_{n,\mathbf{k}}^{(\pm)}$ have the same *uniform* quantum geometric tensor as that of $\Psi_{n,\mathbf{k}}^{(\pm)}$, since the spinor $U_0(\mathbf{r})\chi^{(\pm)}(\mathbf{r})$ is \mathbf{k} independent and normalized at every \mathbf{r} . Equation (10) establishes a LL representation of Bloch states.

To measure the overlap between $\varphi_{m,\mathbf{k}}$ and $\psi_{n,\mathbf{k}}^{(s)}$, we define the LL weight,

$$W_{m,n}^{(s)} = \frac{1}{N} \sum_{\mathbf{k}} |c_{m,n,\mathbf{k}}^{(s)}|^2, \quad (11)$$

where N is the number of \mathbf{k} points. We focus on the first moiré band $\varphi_{1,\mathbf{k}}$, which has a dominant contribution from $\psi_{n,\mathbf{k}}^{(+)}$, since the spinor part of $\psi_{n,\mathbf{k}}^{(+)}$ locally follows the skyrmion field $\Delta(\mathbf{r})$. We numerically find that the weight $W_{1,0}^{(+)}$ on the dressed 0LL wavefunction $\psi_{0,\mathbf{k}}^{(+)}$ is sizable (> 0.6) over a range of twist angle $\theta \in (2.5^\circ, 4.5^\circ)$, as shown in Fig. 1(c). However, $W_{1,0}^{(+)}$ is noticeably below 1 even at θ_m , because the nonuniform quantum geometry of $\varphi_{1,\mathbf{k}}$ is not captured by $\psi_{0,\mathbf{k}}^{(+)}$.

IV. VARIATIONAL MAPPING

To further optimize the weight on the 0LL, we generalize $\psi_{0,\mathbf{k}}^{(+)}(\mathbf{r})$ to $\Theta_{\mathbf{k}}(\mathbf{r})$,

$$\Theta_{\mathbf{k}}(\mathbf{r}) = \mathcal{N}_{\mathbf{k}} U_0(\mathbf{r}) \mathcal{B}(\mathbf{r}) \Psi_{0,\mathbf{k}}^{(-)}(\mathbf{r}), \quad (12)$$

where $\mathcal{B}(\mathbf{r}) = [\mathcal{B}_1(\mathbf{r}), \mathcal{B}_2(\mathbf{r})]^T$ has two components and $\mathcal{N}_{\mathbf{k}}$ is a normalization factor. Here $\mathcal{B}(\mathbf{r})$ is not required to be normalized, but $\Theta_{\mathbf{k}}(\mathbf{r})$ always has a Chern number $\mathcal{C} = 1$ and an ideal but nonuniform quantum geometry, $\tilde{g}_{\mathbf{k}} = \tilde{\Omega}_{\mathbf{k}} \mathbb{1}/2$, where $\tilde{g}_{\mathbf{k}}$ ($\tilde{\Omega}_{\mathbf{k}}$) is the quantum metric (Berry curvature) of $\Theta_{\mathbf{k}}(\mathbf{r})$ [61]. We note that $\Theta_{\mathbf{k}}(\mathbf{r})$ is also the form of wavefunction for the flatbands in twisted bilayer graphene in the chiral limit [58–60].

The advantage of using the generalized 0LL wavefunction $\Theta_{\mathbf{k}}(\mathbf{r})$ are threefolds. First, $\mathcal{B}(\mathbf{r})$ does not need to be an eigenstate of $\Delta(\mathbf{r}) \cdot \sigma$, as the moiré wavefunction does not have to follow the skyrmion field exactly. Second, $\mathcal{B}(\mathbf{r})$ does not need to be normalized, and the spatial variation of $|\mathcal{B}(\mathbf{r})|$ can capture the density modulation. Third, $\Theta_{\mathbf{k}}(\mathbf{r})$ can characterize the nonuniform quantum geometry of the moiré band, while $\psi_{0,\mathbf{k}}^{(+)}$ can not.

We define a new weight $\tilde{W} = \frac{1}{N} \sum_{\mathbf{k}} |\tilde{c}_{\mathbf{k}}|^2$, where $\tilde{c}_{\mathbf{k}} = \langle \varphi_{1,\mathbf{k}} | \Theta_{\mathbf{k}} \rangle$. We maximize \tilde{W} using a variational approach. Taking $\chi^{(+)}(\mathbf{r})$ as an initial ansatz for $\mathcal{B}(\mathbf{r})$, we update $\mathcal{B}(\mathbf{r})$ step-by-step using the gradient ascend method until convergence,

$$\begin{aligned} \text{Re}[\mathcal{B}_i(\mathbf{r})] &\rightarrow \text{Re}[\mathcal{B}_i(\mathbf{r})] + \xi \frac{\delta \tilde{W}}{\delta \text{Re}[\mathcal{B}_i(\mathbf{r})]}, \\ \text{Im}[\mathcal{B}_i(\mathbf{r})] &\rightarrow \text{Im}[\mathcal{B}_i(\mathbf{r})] + \xi \frac{\delta \tilde{W}}{\delta \text{Im}[\mathcal{B}_i(\mathbf{r})]}, \end{aligned} \quad (13)$$

where ξ is a positive parameter (see Appendix B for details).

The maximized \tilde{W} as a function of θ is shown in Fig. 1(c), which has a significant increase compared to $W_{1,0}^{(+)}$ particularly around θ_m . For $\theta \in (2.5^\circ, 3.7^\circ)$, \tilde{W} exceeds 0.9 and achieves a maximum of 0.95 at θ_m . The momentum dependence of $|\tilde{c}_{\mathbf{k}}|$ at θ_m is shown in Fig. 1(d), which is larger than 0.94 for every \mathbf{k} and reaches nearly 1 at the γ point, indicating a high overlap between $\varphi_{1,\mathbf{k}}$ and $\Theta_{\mathbf{k}}$. The spatial variation of $|\mathcal{B}(\mathbf{r})|$ is shown in Fig. 1(e), where the maximal positions form an effective honeycomb lattice, consistent with the density distribution in the first band [31]. Moreover, the quantum geometry fluctuation in $\varphi_{1,\mathbf{k}}(\mathbf{r})$ is qualitatively captured by $\Theta_{\mathbf{k}}(\mathbf{r})$, as illustrated in Fig. 2. We plot the vector field $\tilde{\mathbf{n}}(\mathbf{r})$ defined as $[\mathcal{B}(\mathbf{r})]^\dagger \sigma \mathcal{B}(\mathbf{r})$ in Fig. 3(b) at θ_m . Compared to $\mathbf{n}(\mathbf{r}) = [\chi^{(+)}(\mathbf{r})]^\dagger \sigma \chi^{(+)}(\mathbf{r})$, $\tilde{\mathbf{n}}(\mathbf{r})$ also forms a skyrmion lattice but has spatially varying magnitude.

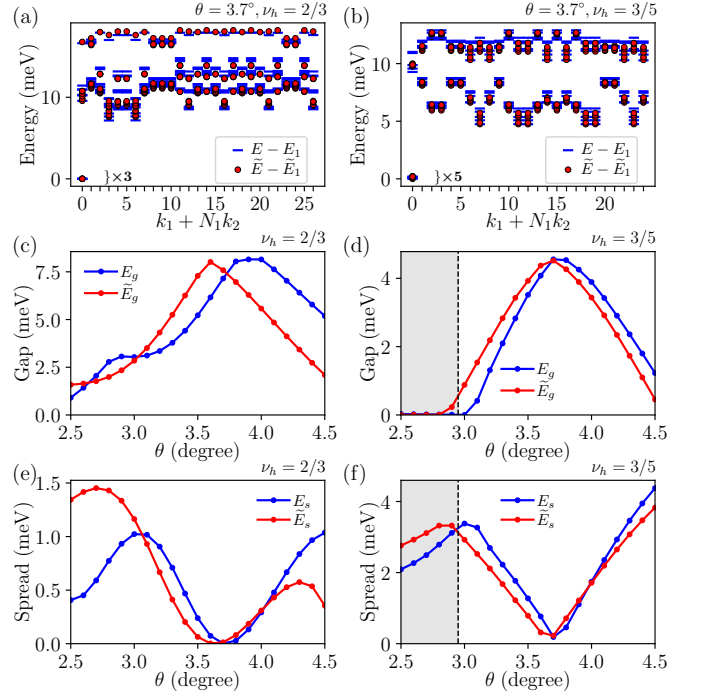


FIG. 4. (a), (b) ED spectra of the original model (blue lines) and variational model (red dots) at $\nu_h = 2/3$ and $3/5$ for $\theta = 3.7^\circ$. (c)-(f) Energy gap E_g and spread E_s as functions of θ at $\nu_h = 2/3$ and $3/5$. Blue (red) lines present results from the original (variational) model. The FCIs are absent in the gray regions of (d) and (f), where E_g is zero.

V. FRACTIONAL CHERN INSULATORS

A remarkable property of the generalized 0LL with $\Theta_{\mathbf{k}}(\mathbf{r})$ is that it allows construction of trial wavefunction for FCIs [59, 61], $\Phi_F = \Psi_F \prod_i U_0(\mathbf{r}_i) \mathcal{B}(\mathbf{r}_i)$, where \mathbf{r}_i is the position of the i th electron and Ψ_F represents the fractional quantum Hall states (or composite Fermi liquid states) in the 0LL. Here Φ_F can be the exact ground state of certain short-range repulsive interactions [61]. The high overlap between $\varphi_{1,\mathbf{k}}$ and $\Theta_{\mathbf{k}}(\mathbf{r})$ provides a rational explanation for FCIs observed in tMoTe₂.

We quantitatively investigate FCIs by studying a many-body Hamiltonian with Coulomb interactions,

$$\hat{\mathcal{H}} = \sum_{\mathbf{k}} (-\mathcal{E}_{\mathbf{k}}) b_{\mathbf{k}}^\dagger b_{\mathbf{k}} + \sum_{\mathbf{k}_1 \mathbf{k}_2 \mathbf{k}_3 \mathbf{k}_4} V_{\mathbf{k}_1 \mathbf{k}_2 \mathbf{k}_3 \mathbf{k}_4} b_{\mathbf{k}_1}^\dagger b_{\mathbf{k}_2}^\dagger b_{\mathbf{k}_3} b_{\mathbf{k}_4}, \quad (14)$$

where we only keep states in the first moiré band at $+K$ valley assuming spontaneous valley polarization, $b_{\mathbf{k}}^\dagger$ ($b_{\mathbf{k}}$) is the creation (annihilation) operator in the *hole* basis, and $-\mathcal{E}_{\mathbf{k}}$ is the hole single-particle energy. The interaction matrix element $V_{\mathbf{k}_1 \mathbf{k}_2 \mathbf{k}_3 \mathbf{k}_4}$ is

$$\begin{aligned} V_{\mathbf{k}_1 \mathbf{k}_2 \mathbf{k}_3 \mathbf{k}_4} &= \frac{1}{2\mathcal{A}} \sum_{\mathbf{q}} V_{\mathbf{q}} M_{\mathbf{k}_1 \mathbf{k}_4}(\mathbf{q}) M_{\mathbf{k}_2 \mathbf{k}_3}(-\mathbf{q}), \\ M_{\mathbf{k} \mathbf{k}'}(\mathbf{q}) &= \int d\mathbf{r} e^{i\mathbf{q} \cdot \mathbf{r}} [f_{\mathbf{k}}(\mathbf{r})]^* f_{\mathbf{k}'}(\mathbf{r}), \end{aligned} \quad (15)$$

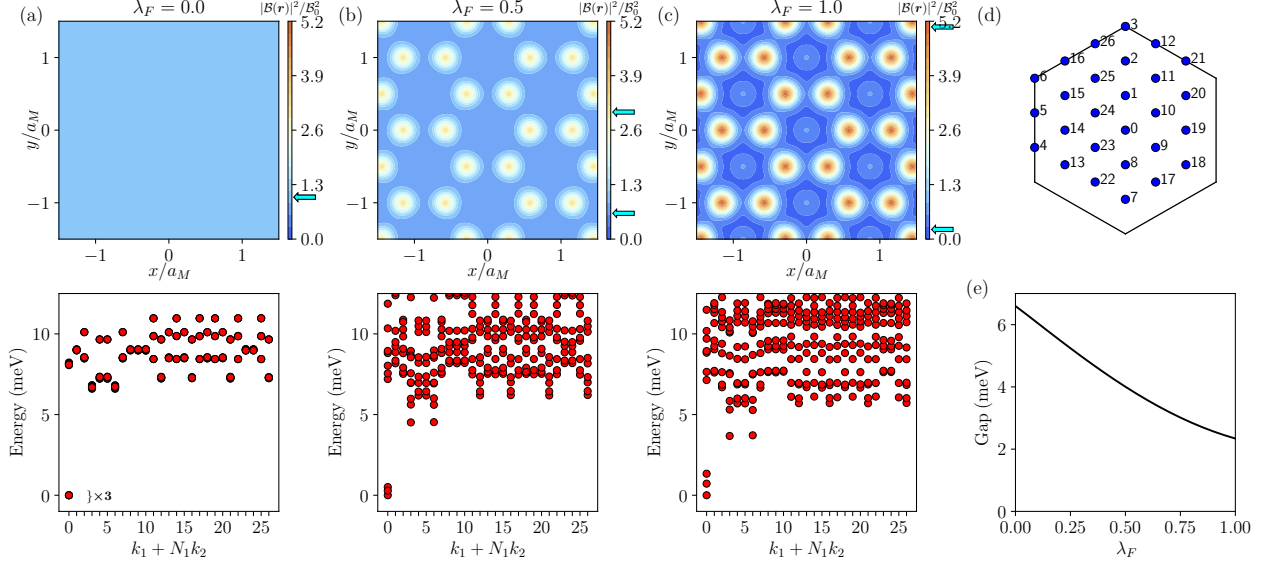


FIG. 5. (a-c) $|\mathcal{B}(\mathbf{r}, \lambda_F)|^2$ scaled by its spatial average (upper panel) and energy spectra (lower panel) for $\lambda_F = 0, 0.5, 1$ at $\nu_h = 2/3$ and $\theta = 2.9^\circ$. (d) The 27-unit-cell momentum clusters used in the ED calculations. The integer numbers are the momentum label $k_1 + N_1 k_2$. (e) Energy gap as a function of λ_F at $\nu_h = 2/3$ and $\theta = 2.9^\circ$.

where \mathcal{A} is the system area, $V_{\mathbf{q}} = 2\pi e^2 \tanh |\mathbf{q}|d/(\epsilon|\mathbf{q}|)$ is gate screened Coulomb interaction, d is the gate-to-sample distance, and ϵ is the dielectric constant. We set $d = 100$ nm and $\epsilon = 5$. In $M_{\mathbf{k}\mathbf{k}'}(\mathbf{q})$, $f_{\mathbf{k}}(\mathbf{r})$ is $[\varphi_{1,\mathbf{k}}(\mathbf{r})]^*$ or $[\Theta_{\mathbf{k}}(\mathbf{r})]^*$, corresponding to the original model and variational model, respectively.

We compare ED spectra of the above two models at $\theta = 3.7^\circ$ in Fig. 4(a) [4(b)] for $\nu_h = 2/3$ (3/5), which are obtained using clusters with 27 (25) unit cells. The three (five) quasi-degenerate ground states in the zero momentum sector indicate the presence of the FCIs for both models at $\nu_h = 2/3$ (3/5) [4, 25, 34]. Moreover, the excited-state spectra of the original model are approximately reproduced by those of the variational model, as shown in Figs. 4(a) and 4(b).

Figure 4 also plots the charge-neutral gap $E_g = E_4 - E_3$ ($E_6 - E_5$) and ground-state energy spread $E_s = E_3 - E_1$ ($E_5 - E_1$) as functions of θ for $\nu_h = 2/3$ (3/5), where E_n is the n th lowest energy in the ED spectra. At $\nu_h = 2/3$, E_g is maximum at $\theta = 3.9^\circ$ (3.6°) in the original (variational) model and is finite for $\theta \in (2.5^\circ, 4.5^\circ)$, indicating a robust FCI phase; E_s is vanishingly small around $\theta = 3.7^\circ$ in both models. The two models also compare quantitatively well at $\nu_h = 3/5$ and share the following features, (1) E_g is maximum and E_s is minimum at $\theta = 3.7^\circ$; (2) E_g is finite only for $\theta \gtrsim 3^\circ$, indicating a narrower range of FCI phase than $\nu_h = 2/3$.

An intriguing observation is that the strongest FCI measured by the maximum E_g or minimum E_s does not occur at θ_m . This can be understood based on the variational wavefunction $\Theta_{\mathbf{k}}(\mathbf{r})$. The spatial variation of

$|\mathcal{B}(\mathbf{r})|$ tends to drive phase transition from FCI to other competing states, weakening the FCI phase if not destroyed. As θ increases, the effect of moiré potential confinement decreases, reducing the spatial variation of $|\mathcal{B}(\mathbf{r})|$. Therefore, the gap E_g at $\nu_h = 2/3$ increases as θ increases away from θ_m , where the effect of bandwidth is minimal. To place this physical argument at a more quantitative level, we expand the periodic function $|\mathcal{B}(\mathbf{r})|^2$ in terms of Fourier series

$$|\mathcal{B}(\mathbf{r})|^2 = \mathcal{B}_0^2 \left(1 + \sum_{\mathbf{g} \neq 0} F_{\mathbf{g}} e^{i\mathbf{g} \cdot \mathbf{r}} \right), \quad (16)$$

where \mathcal{B}_0^2 is the spatial average of $|\mathcal{B}(\mathbf{r})|^2$ and \mathbf{g} represents the moiré reciprocal lattice vectors. \mathcal{B}_0^2 can be absorbed into the normalization factor, so that the Fourier coefficients $F_{\mathbf{g}}$ quantifies the spatial variation and fully determines the interaction matrix element. We note that $\mathcal{B}(\mathbf{r})$ is quasiperiodic with magnetic translational symmetry, but $|\mathcal{B}(\mathbf{r})|$ is periodic.

To clearly illustrate the effect of the spatial variation in $|\mathcal{B}(\mathbf{r})|$, we introduce a parameter λ_F to control the variation as follows,

$$|\mathcal{B}(\mathbf{r}, \lambda_F)|^2 = \mathcal{B}_0^2 \left(1 + \lambda_F \sum_{\mathbf{g} \neq 0} F_{\mathbf{g}} e^{i\mathbf{g} \cdot \mathbf{r}} \right). \quad (17)$$

In the limit of $\lambda_F = 0$, $|\mathcal{B}(\mathbf{r}, \lambda_F)|^2$ is spatially uniform, and the interaction matrix elements become the same as those of lowest Landau level; therefore, the physics of lowest Landau level is fully recovered if the single-particle bandwidth can be further neglected. In the opposite limit

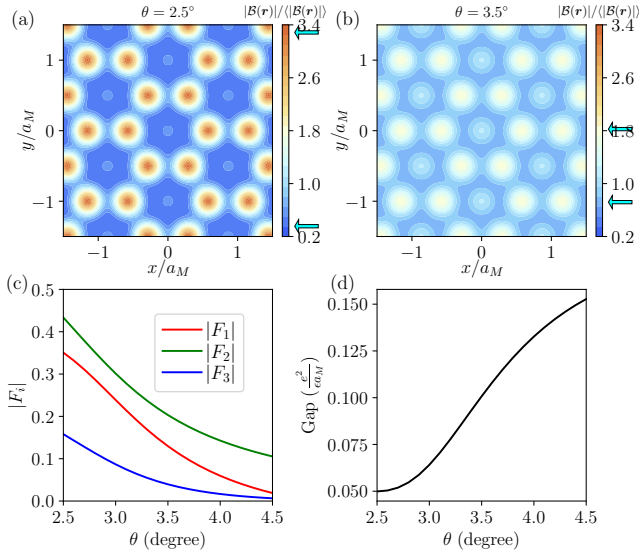


FIG. 6. (a-b) Map of $|\mathcal{B}(\mathbf{r})|$ scaled by its spatial average at $\theta = 2.5^\circ$ and 3.5° . (c) Absolute value of Fourier components $|F_i|$ of $|\mathcal{B}(\mathbf{r})|^2$. (d) Gap as a function of θ at $\nu_h = 2/3$. Here we use $e^2/(\epsilon a_M)$ as the unit of energy, and the single-particle bandwidth is set to 0.

of $\lambda_F = 1$, $|\mathcal{B}(\mathbf{r}, \lambda_F)|^2$ reduces to $|\mathcal{B}(\mathbf{r})|^2$ of the problem under study. The parameter λ_F provides a convenient tuning knob in examining the evolution of the spectrum as the spatial variation of $|\mathcal{B}(\mathbf{r}, \lambda_F)|^2$ changes.

In Figs. 5(a)-(c), we show $|\mathcal{B}(\mathbf{r}, \lambda_F)|^2$ scaled by its spatial average for $\lambda_F = 0, 0.5$, and 1 at $\theta = 2.9^\circ$ in the upper panels, and the corresponding ED energy spectra for the filling factor $\nu_h = 2/3$ in the lower panels. As λ_F increases, the fluctuation of $|\mathcal{B}(\mathbf{r}, \lambda_F)|^2$ increases, and the single-particle wavefunction has larger weights on the maximal points of $|\mathcal{B}(\mathbf{r}, \lambda_F)|^2$. For $\lambda_F = 0$, the energy spectra are essentially the same as those for lowest Landau level at $\nu_h = 2/3$, and host threefold degenerate ground states at the zero momentum sector [momentum cluster shown in Fig. 5(d)] that are separated by an energy gap from excited states, a hallmark of the fractional state. As λ_F increases, the degeneracy in the ground state manifold is gradually broken. Meanwhile, excited states at momentum sectors 3 and 6, which correspond to the Brillouin zone corners as depicted in Fig. 5(d), decrease in energy relative to the ground state. Therefore, the gap between the ground state manifold and excited states decreases as the spatial variation of $|\mathcal{B}(\mathbf{r}, \lambda_F)|^2$ increases, as shown in Fig. 5(e).

The reason behind this numerical observation can be understood as follows. With the increase of the spatial variation of $|\mathcal{B}(\mathbf{r}, \lambda_F)|$, the wavefunction are more concentrated near the maxima positions of $|\mathcal{B}(\mathbf{r}, \lambda_F)|$. The more localized nature of the wavefunction has a tendency to drive phase transition from FCI state to charge density wave (CDW) state. For the results presented in Fig. 5, the ground state remains in the FCI phase, but excited

states at momenta of the Brillouin zone corners come down in energy, which are precursors of CDW phase. This explains the decrease of the gap with the increase of λ_F .

We now consider the twist angle dependence and fix $\lambda_F = 1$. We show the θ dependence of $|\mathcal{B}(\mathbf{r})|$ in Fig. 6(a-b) and the evolution of $|F_i|$ as a function of θ in Fig. 6(c), where F_i denotes the value of the Fourier coefficients of $|\mathcal{B}(\mathbf{r})|^2$ in the i th momentum shell. As θ increases, $|F_i|$ decreases, which results from the weaker moiré confinement at larger twist angles. In Fig. 6(d), we show the charge neutral gap as a function of θ with the bandwidth artificially set to 0, where the gap increases monotonically with increasing θ . When the actual bandwidth is turned on, we find that the gap still increases as θ increases away from the magic angle, but reaches a maximal value at θ around 3.6° , and then decreases. The decrease in the gap for $\theta > 3.6^\circ$ can be attributed to the increase of the bandwidth. Overall, the FCI phase is not the strongest at the magic angle because the spatial variation of $|\mathcal{B}(\mathbf{r})|$ is also strong here. The variational wavefunction provides a convenient way to analyze this effect.

VI. FURTHER APPLICATION

In $t\text{MoTe}_2$, the layer pseudospin skyrmion field can be identified in the Hamiltonian, which leads to an emergent magnetic field and allows us to map Chern bands to Landau levels. Here we generalize our method to the generic case without the emergent magnetic field. We consider a model proposed in Ref. [70]. The Hamiltonian is written as

$$H_\tau(\mathbf{k}) = \begin{pmatrix} \alpha_1 |\mathbf{k}|^2 + \frac{\delta}{2} + V(\mathbf{r}) & v(\tau k_x - i k_y) \\ v(\tau k_x + i k_y) & -\alpha_2 |\mathbf{k}|^2 - \frac{\delta}{2} + V(\mathbf{r}) \end{pmatrix} \quad (18)$$

which describes a narrow gap semiconductor in a superlattice potential $V(\mathbf{r}) = 2V_0 \sum_{n=1}^3 \cos(\mathbf{g}_n \cdot \mathbf{r} + \phi)$ with $\mathbf{g}_n = g(-\cos \frac{2\pi n}{3}, \sin \frac{2\pi n}{3})$, $g = 4\pi/\sqrt{3}a$, and a being the superlattice period. Here $\tau = \pm$ is the spin index. This model can host a Chern band that nearly saturates the trace inequality $T \geq 0$ in certain parameter regimes, but no skyrmion field or emergent magnetic field can be identified in the Hamiltonian. We take $\phi = \pi$, $\alpha_1 = \alpha_2 = \alpha$, $g/k_D = 2$ and $V_0/E_D = 1.5$ in our calculation, where $k_D = \nu/\alpha$ and $E_D = \nu^2/\alpha$ are characteristic momentum and energy, respectively.

Figure 7(a) shows the band structure at $\tau = -$ and $\delta/E_D = 4.4$, where the first conduction band is energetically isolated from other bands and nearly flat with a Chern number of +1. We further show the deviation T from the ideal quantum geometry in Fig. 7(b) for $\delta/E_D \in [3.0, 4.8]$, where T can be as small as 0.18. The small value of T indicates the resemblance of the Chern band with the generalized OLL, of which the wavefunction $\Theta_{\mathbf{k}}(\mathbf{r})$ takes the same form as in Eq. (12). For this case,

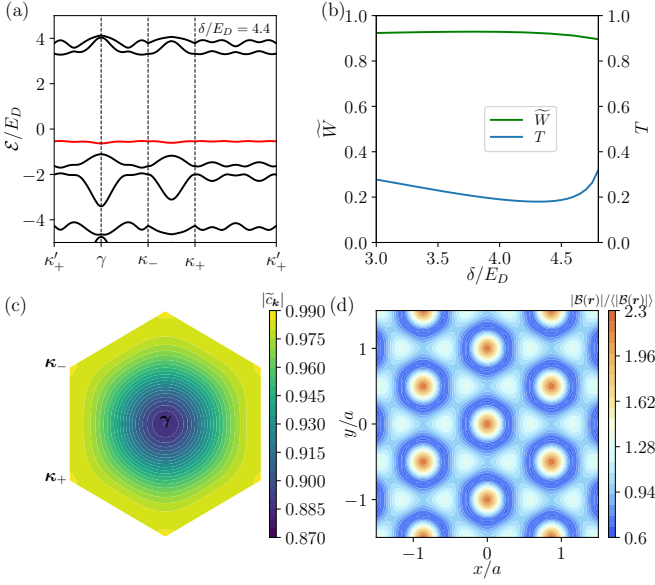


FIG. 7. (a) Band structure of the model Hamiltonian $H_\tau(\mathbf{k})$ at $\delta/E_D = 4.4$ and $\tau = -$. The first conduction band is plotted in red line. (b) Landau-level weight \tilde{W} and deviation from ideal quantum geometry T of the first conduction band as a function of δ/E_D . (c) Overlap $|\tilde{c}_{\mathbf{k}}|$ in the Brillouin zone. (d) Map of $|\mathcal{B}(\mathbf{r})|$ scaled by its spatial average. $\delta/E_D = 4.4$ in (c) and (d).

$U_0(\mathbf{r})$ is taken to be an identity matrix and $\mathcal{B}(\mathbf{r})$ also has two components. We again quantify the resemblance by defining the Landau Level weight $\tilde{W} = \frac{1}{N} \sum_{\mathbf{k}} |\tilde{c}_{\mathbf{k}}|^2$, where $\tilde{c}_{\mathbf{k}} = \langle \varphi_{\mathbf{k}} | \Theta_{\mathbf{k}} \rangle$ and $\varphi_{\mathbf{k}}$ is the two-component wavefunction for the first conduction band of $H_\tau(\mathbf{k})$ with $\tau = -$. We take the following initial ansatz for $\mathcal{B}(\mathbf{r})$,

$$\mathcal{B}(\mathbf{r}) \rightarrow \frac{\varphi_\gamma(\mathbf{r})}{|\varphi_\gamma(\mathbf{r})|^2} \Psi_{0,\gamma}^{(+)}(\mathbf{r}), \quad (19)$$

where $\varphi_\gamma(\mathbf{r})$ is the wavefunction of the first conduction band at the γ point. With this ansatz, we update $\mathcal{B}(\mathbf{r})$ step-by-step by the gradient ascend method until convergence. As presented in Fig. 7(b), the optimized \tilde{W} is over 0.9 for $\delta/E_D \in [3.0, 4.8]$. In Fig. 7(c), we plot $|\tilde{c}_{\mathbf{k}}|$ over the Brillouin zone at $\delta/E_D = 4.4$, where $|\tilde{c}_{\mathbf{k}}|$ is nearly 1 at the Brillouin zone corners. We further plot $|\mathcal{B}(\mathbf{r})|$ in Fig. 7(d), which is a continuous function of \mathbf{r} and respects the symmetry of the system. This example demonstrates that our method is general in mapping the Chern band to generalized Landau levels.

VII. DISCUSSION

Small values of the deviation T from the ideal quantum geometry have often been interpreted as an indication of the resemblance between Chern bands and the generalized 0LL, but the exact form of the latter is unknown

(i.e., unknown $\mathcal{B}(\mathbf{r})$). Our work provides a variation approach to determine the optimized $\mathcal{B}(\mathbf{r})$ and quantify the resemblance. In $t\text{MoTe}_2$, we show that the variational wavefunction $\Theta_{\mathbf{k}}(\mathbf{r})$ successfully captures both the single-particle and many-body physics about the formation and properties of FCIs. We expect applications of our theory in several directions. First, the wavefunction Φ_F can be generalized to excited states of fractionalized quasihole and quasielectron [72]. After $\Theta_{\mathbf{k}}(\mathbf{r})$ is determined using the variational approach, properties of anyon excitations in FCIs can be explored based on many-body wavefunctions. Second, the variational mapping between moiré bands and higher-index LL can be performed using our approach combined with the recently proposed theory of generalized LL [73]. Several theoretical works reported non-Abelian fractional states at half-filling of the second moiré band [43–46], whose connection to the first LL can be worked out. Finally, FCIs at zero magnetic field have also been observed in a rhombohedral pentalayer graphene–hBN moiré superlattice [12] and theoretically proposed in various models [70, 74–76]. Our mapping strategy can be readily applied to different systems to reveal the properties of FCIs.

VIII. ACKNOWLEDGMENTS

We thank Jie Wang and Zhao Liu for their valuable discussions. This work is supported by National Natural Science Foundation of China (Grant No. 12274333), and National Key Research and Development Program of China (Grants No. 2021YFA1401300 and No. 2022YFA1402401). The numerical calculations in this paper have been performed on the supercomputing system in the Supercomputing Center of Wuhan University.

Appendix A: Symmetry

This appendix presents the symmetry properties of different quantities. We study both point group symmetries and translational symmetry. The translation symmetry is generated by primitive lattice vectors $\mathbf{a}_{1,2} = (\pm \frac{\sqrt{3}}{2}, \frac{1}{2})a_M$ of the moiré triangular lattice.

We first study the symmetry properties of magnetic Bloch wavefunctions at the zeroth Landau level, which takes the following form under symmetric gauge,

$$\begin{aligned} \Psi_{0,\mathbf{k}}^{(-)}(\mathbf{r}) &= \frac{1}{S_{\mathbf{k}}\ell} \sigma(z + iz_{\mathbf{k}}\ell^2) e^{-\frac{1}{4}|z_{\mathbf{k}}|^2\ell^2 - \frac{1}{4}|z|^2\ell^{-2} + \frac{i}{2}z_{\mathbf{k}}^*z}, \\ \Psi_{0,\mathbf{k}}^{(+)}(\mathbf{r}) &= [\Psi_{0,-\mathbf{k}}^{(-)}(\mathbf{r})]^*. \end{aligned} \quad (\text{A1})$$

where $z = x + iy$, $z_{\mathbf{k}} = k_x + ik_y$, $S_{\mathbf{k}}$ is a normalization factor, $\ell = \sqrt{\mathcal{A}_0/(2\pi)}$, and \mathcal{A}_0 is the area of the (magnetic) unit cell. The modified Weierstrass sigma function

$\sigma(z)$ is [77]

$$\sigma(z) = ze^{\frac{\eta_1 z^2}{z_1}} \frac{\theta_1(u|\tau)}{u\theta_1'(0|\tau)}, \quad (\text{A2})$$

where $\theta_1(u|\tau)$ is the Jacobi theta function, $u = \pi z/z_1$, $\eta_1 = z_1^*/(4\ell^2)$, $\tau = z_2/z_1$, and $z_j = a_{j,x} + ia_{j,y}$. Expression of $\theta_1(u|\tau)$ is

$$\theta_1(u|\tau) = - \sum_{n=-\infty}^{+\infty} e^{i\pi\tau(n+\frac{1}{2})^2} e^{2\pi i(n+1/2)(u+1/2)}. \quad (\text{A3})$$

The magnetic Bloch wavefunction satisfies the following magnetic translational symmetry in real space,

$$\Psi_{0,\mathbf{k}}^{(s)}(\mathbf{r} + \mathbf{a}_i) = -e^{-i\frac{1}{2\ell^2}\mathbf{s}\mathbf{a}_i \times \mathbf{r}} e^{i\mathbf{k} \cdot \mathbf{a}_i} \Psi_{0,\mathbf{k}}^{(s)}(\mathbf{r}). \quad (\text{A4})$$

In momentum space, the magnetic Bloch wavefunction satisfies a quasi-periodic boundary condition,

$$\Psi_{0,\mathbf{k}+\mathbf{b}_i}^{(s)}(\mathbf{r}) = -e^{-i\frac{\ell^2}{2}\mathbf{s}\mathbf{b}_i \times \mathbf{k}} \Psi_{0,\mathbf{k}}^{(s)}(\mathbf{r}), \quad (\text{A5})$$

where $\mathbf{b}_{1,2} = \frac{4\pi}{\sqrt{3}a_M}(\pm\frac{1}{2}, \frac{\sqrt{3}}{2})$ are primitive reciprocal lattice vectors and $\mathbf{a}_i \cdot \mathbf{b}_j = 2\pi\delta_{ij}$.

It is also useful to consider the original definition of Weierstrass sigma function,

$$\sigma(z) = z \prod_{w \in \Lambda} (1 - \frac{z}{w}) \exp(\frac{z}{w} + \frac{z^2}{2w^2}), \quad (\text{A6})$$

where $\Lambda = \{mz_1 + nz_2 \mid m \in \mathbb{Z}, n \in \mathbb{Z}, (m,n) \neq (0,0)\}$. It is known that two forms in Eqs. (A2) and (A6) are equivalent in a triangular lattice system [77]. Based on Eq. (A6), we derive the point group symmetry of magnetic Bloch wavefunction at three high symmetry momenta $\boldsymbol{\gamma} = (0,0)$, $\boldsymbol{\kappa}_+ = \frac{4\pi}{3a_M}(-\frac{\sqrt{3}}{2}, -\frac{1}{2})$, and $\boldsymbol{\kappa}_- = \frac{4\pi}{3a_M}(-\frac{\sqrt{3}}{2}, +\frac{1}{2})$.

$$\begin{aligned} \Psi_{0,\boldsymbol{\gamma}}^{(s)}(\hat{R}_{3z}\mathbf{r}) &= e^{-i\frac{2}{3}\pi s} \Psi_{0,\boldsymbol{\gamma}}^{(s)}(\mathbf{r}), \\ \Psi_{0,\boldsymbol{\gamma}}^{(s)}(\hat{R}_{2z}\mathbf{r}) &= -\Psi_{0,\boldsymbol{\gamma}}^{(s)}(\mathbf{r}), \\ \Psi_{0,\boldsymbol{\gamma}}^{(s)}(\hat{M}_x\mathbf{r}) &= -[\Psi_{0,\boldsymbol{\gamma}}^{(s)}(\mathbf{r})]^*, \\ \Psi_{0,\boldsymbol{\kappa}_\pm}^{(s)}(\hat{R}_{3z}\mathbf{r}) &= \Psi_{0,\boldsymbol{\kappa}_\pm}^{(s)}(\mathbf{r}), \\ \Psi_{0,\boldsymbol{\kappa}_\pm}^{(s)}(\hat{R}_{2z}\mathbf{r}) &= -e^{\pm i\frac{2}{3}\pi s} \Psi_{0,\boldsymbol{\kappa}_\mp}^{(s)}(\mathbf{r}), \\ \Psi_{0,\boldsymbol{\kappa}_\pm}^{(s)}(\hat{M}_x\mathbf{r}) &= -[\Psi_{0,\boldsymbol{\kappa}_\mp}^{(s)}(\mathbf{r})]^*, \end{aligned} \quad (\text{A7})$$

where \hat{R}_{nz} represents the n -fold rotation around the z -axis and \hat{M}_x is the mirror operation that flips x to $-x$.

We turn to the moiré Hamiltonian H of $t\text{MoTe}_2$, which is invariant under \hat{C}_{3z} , $\hat{C}_{2y}\hat{T}$, and an effective inversion symmetry $\hat{\mathcal{I}}$, where \hat{C}_{nj} represents n -fold rotational symmetry around j axis and \hat{T} is the time-reversal symmetry. Here \hat{C}_{2y} is a combination of \hat{M}_x and layer exchange σ_x , where σ_x is the x Pauli matrix in the layer pseudospin space. Both \hat{C}_{3z} and $\hat{C}_{2y}\hat{T}$ symmetries are derived from

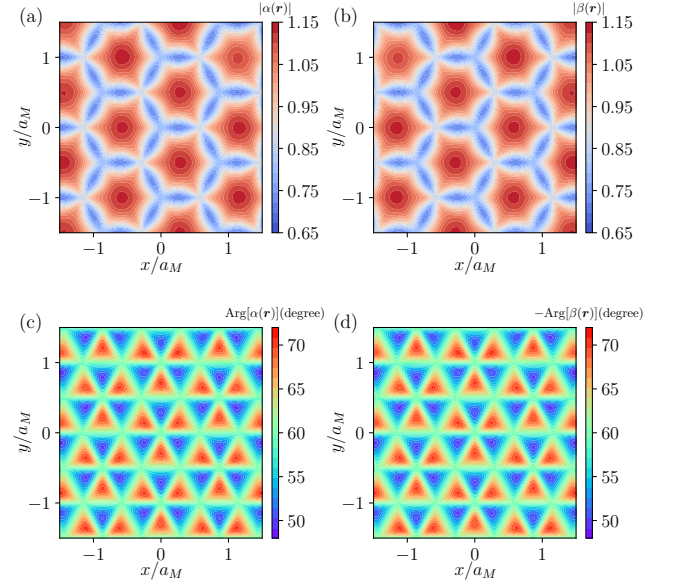


FIG. 8. (a), (b) Spatial distribution of amplitudes $|\alpha(\mathbf{r})|$ and $|\beta(\mathbf{r})|$. (c), (d) Spatial distribution of phases $\text{Arg}[\alpha(\mathbf{r})]$ and $-\text{Arg}[\beta(\mathbf{r})]$.

point group symmetries of $t\text{MoTe}_2$. On the other hand, $\hat{\mathcal{I}}$ is an emergent symmetry of the low-energy effective Hamiltonian H , and $\hat{\mathcal{I}}$ is a combination of \hat{R}_{2z} and layer exchange σ_x .

The scalar potential $\Delta_0(\mathbf{r})$ and the layer pseudospin field $\boldsymbol{\Delta}(\mathbf{r})$ are defined as

$$\begin{aligned} \Delta_0(\mathbf{r}) &= \frac{\Delta_+(\mathbf{r}) + \Delta_-(\mathbf{r})}{2}, \\ \boldsymbol{\Delta}(\mathbf{r}) &= [\text{Re} \tilde{\Delta}_t^\dagger(\mathbf{r}), \text{Im} \tilde{\Delta}_t^\dagger(\mathbf{r}), \frac{\Delta_+(\mathbf{r}) - \Delta_-(\mathbf{r})}{2}], \quad (\text{A8}) \\ \tilde{\Delta}_t^\dagger(\mathbf{r}) &= e^{i(\boldsymbol{\kappa}_+ - \boldsymbol{\kappa}_-) \cdot \mathbf{r}} \Delta_t^\dagger(\mathbf{r}). \end{aligned}$$

$\boldsymbol{\Delta}(\mathbf{r})$ transforms under R_{3z} , R_{2z} , M_x and translational operations as follows,

$$\begin{aligned} \boldsymbol{\Delta}(\hat{R}_{3z}\mathbf{r}) &= \boldsymbol{\Delta}(\mathbf{r}), \\ \boldsymbol{\Delta}(\hat{R}_{2z}\mathbf{r}) &= [\Delta_x(\mathbf{r}), -\Delta_y(\mathbf{r}), -\Delta_z(\mathbf{r})], \\ \boldsymbol{\Delta}(\hat{M}_x\mathbf{r}) &= [\Delta_x(\mathbf{r}), \Delta_y(\mathbf{r}), -\Delta_z(\mathbf{r})], \\ \Delta_z(\mathbf{r} + \mathbf{a}_i) &= \Delta_z(\mathbf{r}), \\ \Delta_x(\mathbf{r} + \mathbf{a}_i) \pm i\Delta_y(\mathbf{r} + \mathbf{a}_i) &= e^{\pm i(\boldsymbol{\kappa}_+ - \boldsymbol{\kappa}_-) \cdot \mathbf{a}_i} [\Delta_x(\mathbf{r}) \pm i\Delta_y(\mathbf{r})]. \end{aligned} \quad (\text{A9})$$

We then consider the symmetries of $\alpha(\mathbf{r})$ and $\beta(\mathbf{r})$,

which are defined as

$$\begin{aligned}\alpha(\mathbf{r}) &= \frac{e^{-i\zeta(\mathbf{r})/2}}{|\Psi_{0,\kappa_-}^{(+)}(\mathbf{r})|} \sqrt{\frac{1+n_z(\mathbf{r})}{2}}, \\ \beta(\mathbf{r}) &= \frac{e^{i\zeta(\mathbf{r})/2}}{|\Psi_{0,\kappa_+}^{(+)}(\mathbf{r})|} \sqrt{\frac{1-n_z(\mathbf{r})}{2}}, \\ \zeta(\mathbf{r}) &= \text{Arg}\left\{ \frac{n_x(\mathbf{r}) + in_y(\mathbf{r})}{[\Psi_{0,\kappa_-}^{(+)}(\mathbf{r})]^* \Psi_{0,\kappa_+}^{(+)}(\mathbf{r})} \right\}.\end{aligned}\quad (\text{A10})$$

Here $n_j(\mathbf{r}) = \Delta_j(\mathbf{r})/|\Delta(\mathbf{r})|$. Using Eqs. (A4), (A7) and (A9), we have

$$\begin{aligned}\zeta(\hat{R}_{3z}\mathbf{r}) &= \zeta(\mathbf{r}), \\ \zeta(\hat{R}_{2z}\mathbf{r}) &= -\zeta(\mathbf{r}) - \frac{4}{3}\pi, \\ \zeta(\hat{M}_x\mathbf{r}) &= \zeta(\mathbf{r}), \\ \zeta(\mathbf{r} + \mathbf{a}_i) &= \zeta(\mathbf{r}),\end{aligned}\quad (\text{A11})$$

$$\begin{aligned}\alpha(\hat{R}_{3z}\mathbf{r}) &= \alpha(\mathbf{r}), \beta(\hat{R}_{3z}\mathbf{r}) = \beta(\mathbf{r}), \\ \alpha(\hat{R}_{2z}\mathbf{r}) &= e^{i\frac{2}{3}\pi}\beta(\mathbf{r}), \beta(\hat{R}_{2z}\mathbf{r}) = e^{-i\frac{2}{3}\pi}\alpha(\mathbf{r}), \\ \alpha(\hat{M}_x\mathbf{r}) &= \beta^*(\mathbf{r}), \beta(\hat{M}_x\mathbf{r}) = \alpha^*(\mathbf{r}), \\ \alpha(\mathbf{r} + \mathbf{a}_i) &= \alpha(\mathbf{r}), \beta(\mathbf{r} + \mathbf{a}_i) = \beta(\mathbf{r}).\end{aligned}\quad (\text{A12})$$

We emphasize that $\alpha(\mathbf{r})$ and $\beta(\mathbf{r})$ are periodic functions with the moiré lattice periodicity. We plot the amplitude and phase of $\alpha(\mathbf{r})$ and $\beta(\mathbf{r})$ in Fig. 8, where the symmetry constraints in Eq. (A12) are obeyed.

The spinors $\chi^{(s)}(\mathbf{r})$ are defined as

$$\begin{aligned}\chi^{(+)}(\mathbf{r}) &= \{\alpha(\mathbf{r})\Psi_{0,\kappa_-}^{(+)}(\mathbf{r}), \beta(\mathbf{r})\Psi_{0,\kappa_+}^{(+)}(\mathbf{r})\}^T, \\ \chi^{(-)}(\mathbf{r}) &= \{\beta^*(\mathbf{r})[\Psi_{0,\kappa_+}^{(+)}(\mathbf{r})]^*, -\alpha^*(\mathbf{r})[\Psi_{0,\kappa_-}^{(+)}(\mathbf{r})]^*\}^T.\end{aligned}\quad (\text{A13})$$

The transformation of $\chi^{(s)}(\mathbf{r})$ under symmetry operations is given by,

$$\begin{aligned}\chi^{(s)}(\hat{R}_{3z}\mathbf{r}) &= \chi^{(s)}(\mathbf{r}), \\ \chi^{(s)}(\hat{R}_{2z}\mathbf{r}) &= -s\sigma_x\chi^{(s)}(\mathbf{r}), \\ \chi^{(s)}(\hat{M}_x\mathbf{r}) &= -s\sigma_x[\chi^{(s)}(\mathbf{r})]^*, \\ \chi^{(+)}(\mathbf{r} + \mathbf{a}_i) &= -e^{-i\frac{1}{2\ell^2}\mathbf{a}_i \times \mathbf{r}} \tilde{U}_0(\mathbf{a}_i)\chi^{(+)}(\mathbf{r}), \\ \chi^{(-)}(\mathbf{r} + \mathbf{a}_i) &= -e^{i\frac{1}{2\ell^2}\mathbf{a}_i \times \mathbf{r}} U_0^\dagger(\mathbf{a}_i)\chi^{(-)}(\mathbf{r}),\end{aligned}\quad (\text{A14})$$

where $\tilde{U}_0(\mathbf{r}) = \text{diag}(e^{i\kappa_- \cdot \mathbf{r}}, e^{i\kappa_+ \cdot \mathbf{r}})$. We note that $\chi^{(s)}(\mathbf{r})$ obey magnetic translational symmetry.

The dressed Landau-level wavefunctions are given by

$$\begin{aligned}\psi_{n,\mathbf{k}}^{(+)}(\mathbf{r}) &= U_0(\mathbf{r})\chi^{(+)}(\mathbf{r})\Psi_{n,\mathbf{k}}^{(-)}(\mathbf{r}), \\ \psi_{n,\mathbf{k}}^{(-)}(\mathbf{r}) &= U_0(\mathbf{r})\chi^{(-)}(\mathbf{r})\Psi_{n,\mathbf{k}}^{(+)}(\mathbf{r}).\end{aligned}\quad (\text{A15})$$

Here $\Psi_{n,\mathbf{k}}^{(s)}(\mathbf{r})$ is the wavefunction for the n th Landau level and satisfies the magnetic translational symmetry,

$$\Psi_{n,\mathbf{k}}^{(s)}(\mathbf{r} + \mathbf{a}_i) = -e^{-i\frac{1}{2\ell^2}s\mathbf{a}_i \times \mathbf{r}} e^{i\mathbf{k} \cdot \mathbf{a}_i} \Psi_{n,\mathbf{k}}^{(s)}(\mathbf{r}). \quad (\text{A16})$$

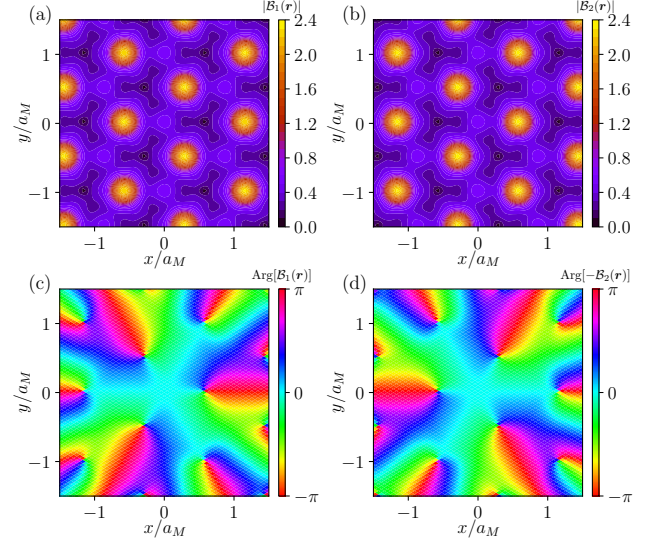


FIG. 9. Spatial distribution of (a) $|\mathcal{B}_1(\mathbf{r})|$, (b) $|\mathcal{B}_2(\mathbf{r})|$, (c) $\text{Arg}[\mathcal{B}_1(\mathbf{r})]$, and (d) $\text{Arg}[-\mathcal{B}_2(\mathbf{r})]$ for $\theta = 2.9^\circ$.

The combination of $U_0(\mathbf{r})\chi^{(s)}(\mathbf{r})$ and $\Psi_{0,\mathbf{k}}^{(-s)}(\mathbf{r})$ leads to normal translational symmetry,

$$\psi_{n,\mathbf{k}}^{(s)}(\mathbf{r} + \mathbf{a}_i) = e^{i\mathbf{k} \cdot \mathbf{a}_i} \psi_{n,\mathbf{k}}^{(s)}(\mathbf{r}). \quad (\text{A17})$$

Therefore, $\psi_{n,\mathbf{k}}^{(s)}(\mathbf{r})$ are Bloch wavefunctions.

Point group symmetries for the dressed zeroth Landau-level wavefunctions at the three high-symmetry momenta are given by

$$\begin{aligned}\hat{C}_{3z}[U_0^\dagger(\mathbf{r})\psi_{0,\gamma}^{(s)}(\mathbf{r})] &= e^{i\frac{2}{3}\pi s}[U_0^\dagger(\mathbf{r})\psi_{0,\gamma}^{(s)}(\mathbf{r})], \\ \hat{C}_{2y}\hat{T}[U_0^\dagger(\mathbf{r})\psi_{0,\gamma}^{(s)}(\mathbf{r})] &= s[U_0^\dagger(\mathbf{r})\psi_{0,\gamma}^{(s)}(\mathbf{r})], \\ \hat{I}[U_0^\dagger(\mathbf{r})\psi_{0,\gamma}^{(s)}(\mathbf{r})] &= s[U_0^\dagger(\mathbf{r})\psi_{0,\gamma}^{(s)}(\mathbf{r})], \\ \hat{C}_{3z}[U_0^\dagger(\mathbf{r})\psi_{0,\kappa_\pm}^{(s)}(\mathbf{r})] &= U_0^\dagger(\mathbf{r})\psi_{0,\kappa_\pm}^{(s)}(\mathbf{r}), \\ \hat{C}_{2y}\hat{T}[U_0^\dagger(\mathbf{r})\psi_{0,\kappa_\pm}^{(s)}(\mathbf{r})] &= s[U_0^\dagger(\mathbf{r})\psi_{0,\kappa_\mp}^{(s)}(\mathbf{r})], \\ \hat{I}[U_0^\dagger(\mathbf{r})\psi_{0,\kappa_\pm}^{(s)}(\mathbf{r})] &= s e^{\mp i\frac{2}{3}\pi s}[U_0^\dagger(\mathbf{r})\psi_{0,\kappa_\mp}^{(s)}(\mathbf{r})].\end{aligned}\quad (\text{A18})$$

Here $\hat{C}_{3z} = \hat{R}_{3z}$, $\hat{C}_{2y}\hat{T} = \sigma_x \hat{M}_x \mathcal{K}$, $\hat{I} = \sigma_x \hat{R}_{2z}$, and \mathcal{K} is the complex conjugation operator.

The original moiré Hamiltonian H has the moiré periodicity. The point group symmetries are revealed more clearly using $H_1 = U_0^\dagger(\mathbf{r})H U_0(\mathbf{r})$,

$$\begin{aligned}\hat{C}_{3z}H_1(\mathbf{r})\hat{C}_{3z}^{-1} &\equiv H_1(\hat{R}_{3z}\mathbf{r}) = H_1(\mathbf{r}), \\ [\hat{C}_{2y}\hat{T}]H_1(\mathbf{r})[\hat{C}_{2y}\hat{T}]^{-1} &\equiv \sigma_x H_1^*(\hat{M}_x\mathbf{r})\sigma_x = H_1(\mathbf{r}) \\ \hat{I}H_1(\mathbf{r})\hat{I}^{-1} &\equiv \sigma_x H_1(\hat{R}_{2z}\mathbf{r})\sigma_x = H_1(\mathbf{r}).\end{aligned}\quad (\text{A19})$$

We find that the Bloch wavefunction $\varphi_{1,\mathbf{k}}(\mathbf{r})$ of the first moiré band of H has the following symmetry repre-

sensation at high-symmetry momenta,

$$\begin{aligned}\hat{C}_{3z}[U_0^\dagger(\mathbf{r})\varphi_{1,\gamma}(\mathbf{r})] &= e^{i\frac{2}{3}\pi}[U_0^\dagger(\mathbf{r})\varphi_{1,\gamma}(\mathbf{r})], \\ \hat{\mathcal{I}}[U_0^\dagger(\mathbf{r})\varphi_{1,\gamma}(\mathbf{r})] &= +[U_0^\dagger(\mathbf{r})\varphi_{1,\gamma}(\mathbf{r})], \\ \hat{C}_{3z}[U_0^\dagger(\mathbf{r})\varphi_{1,\kappa_\pm}(\mathbf{r})] &= +[U_0^\dagger(\mathbf{r})\varphi_{1,\kappa_\pm}(\mathbf{r})].\end{aligned}\quad (\text{A20})$$

By comparing Eqs. (A18) and (A20), we conclude that the dressed zeroth Landau-level wavefunction $\psi_{0,\mathbf{k}}^{(+)}(\mathbf{r})$ consistently captures the symmetry representation of the first moiré band wavefunction $\varphi_{1,\mathbf{k}}(\mathbf{r})$.

Under lattice translation, H_1 transforms as follows,

$$H_1(\mathbf{r} + \mathbf{a}_i) = U_0^\dagger(\mathbf{a}_i)H_1(\mathbf{r})U_0(\mathbf{a}_i). \quad (\text{A21})$$

In the local frame of $\Delta(\mathbf{r})$, the Hamiltonian is transformed to $H_2 = U^\dagger(\mathbf{r})H_1U(\mathbf{r})$, where $U(\mathbf{r}) = (\chi^{(+)}(\mathbf{r}), \chi^{(-)}(\mathbf{r}))$. The transformation of $U(\mathbf{r})$ under lattice translation is,

$$U(\mathbf{r} + \mathbf{a}_i) = -U_0^\dagger(\mathbf{a}_i)U(\mathbf{r})U_m(\mathbf{r}) \quad (\text{A22})$$

where $U_m(\mathbf{r})$ is

$$U_m(\mathbf{r}) = \begin{pmatrix} e^{-i\frac{1}{2\ell^2}\mathbf{a}_i \times \mathbf{r}} & 0 \\ 0 & e^{i\frac{1}{2\ell^2}\mathbf{a}_i \times \mathbf{r}} \end{pmatrix} \quad (\text{A23})$$

Therefore, H_2 has the following translational symmetry,

$$H_2(\mathbf{r} + \mathbf{a}_i) = U_m^\dagger(\mathbf{r})H_2(\mathbf{r})U_m(\mathbf{r}). \quad (\text{A24})$$

We plot in Fig. 9 the spatial distribution of $|\mathcal{B}_1(\mathbf{r})|$, $|\mathcal{B}_2(\mathbf{r})|$, $\text{Arg}[\mathcal{B}_1(\mathbf{r})]$ and $\text{Arg}[-\mathcal{B}_2(\mathbf{r})]$ for $\theta = 2.9^\circ$. We note that $\mathcal{B}(\mathbf{r})$ inherits the symmetries of $\chi^{(+)}(\mathbf{r})$.

Appendix B: Variational method

The details of the variational method are described as follows. The expression of $\tilde{c}_{\mathbf{k}}$ is given by

$$\begin{aligned}\tilde{c}_{\mathbf{k}} &= \langle \varphi_{1,\mathbf{k}} | \Theta_{\mathbf{k}} \rangle \\ &= \frac{\sum_{i=1,2} \int_{\mathcal{A}_0} d\mathbf{r} \varphi_{1,\mathbf{k},i}^*(\mathbf{r}) [U_0(\mathbf{r})]_{ii} \mathcal{B}_i(\mathbf{r}) \Psi_{0,\mathbf{k}}^{(-)}(\mathbf{r})}{\sqrt{\int_{\mathcal{A}_0} d\mathbf{r} |\mathcal{B}(\mathbf{r})|^2 |\Psi_{0,\mathbf{k}}^{(-)}(\mathbf{r})|^2} \sqrt{\int_{\mathcal{A}_0} d\mathbf{r} |\varphi_{1,\mathbf{k}}(\mathbf{r})|^2}} \\ &= \frac{\sum_{i=1,2} \sum_{\mathbf{r}} \varphi_{1,\mathbf{k},i}^*(\mathbf{r}) [U_0(\mathbf{r})]_{ii} \mathcal{B}_i(\mathbf{r}) \Psi_{0,\mathbf{k}}^{(-)}(\mathbf{r})}{\sqrt{\sum_{\mathbf{r}} |\mathcal{B}(\mathbf{r})|^2 |\Psi_{0,\mathbf{k}}^{(-)}(\mathbf{r})|^2}}\end{aligned}\quad (\text{B1})$$

where we take the normalization $\sum_{\mathbf{r}} |\varphi_{1,\mathbf{k}}(\mathbf{r})|^2 = 1$, with discretized summation within a unit cell. The weight \tilde{W} takes the form

$$\begin{aligned}\tilde{W} &= \frac{1}{N} \sum_{\mathbf{k}} |\tilde{c}_{\mathbf{k}}|^2 = \frac{1}{N} \sum_{\mathbf{k}} \frac{|u_{\mathbf{k}}|^2}{v_{\mathbf{k}}}, \\ u_{\mathbf{k}} &= \sum_{i=1,2} \sum_{\mathbf{r}} \varphi_{1,\mathbf{k},i}^*(\mathbf{r}) [U_0(\mathbf{r})]_{ii} \mathcal{B}_i(\mathbf{r}) \Psi_{0,\mathbf{k}}^{(-)}(\mathbf{r}), \\ v_{\mathbf{k}} &= \sum_{\mathbf{r}} |\mathcal{B}(\mathbf{r})|^2 |\Psi_{0,\mathbf{k}}^{(-)}(\mathbf{r})|^2.\end{aligned}\quad (\text{B2})$$

The gradients of $u_{\mathbf{k}}$ and $v_{\mathbf{k}}$ with respect to $\mathcal{B}_i(\mathbf{r})$ are

$$\begin{aligned}\frac{\delta u_{\mathbf{k}}}{\delta \text{Re}[\mathcal{B}_i(\mathbf{r})]} &= \varphi_{1,\mathbf{k},i}^* [U_0(\mathbf{r})]_{ii} \Psi_{0,\mathbf{k}}^{(-)}(\mathbf{r}), \\ \frac{\delta u_{\mathbf{k}}}{\delta \text{Im}[\mathcal{B}_i(\mathbf{r})]} &= i \varphi_{1,\mathbf{k},i}^* [U_0(\mathbf{r})]_{ii} \Psi_{0,\mathbf{k}}^{(-)}(\mathbf{r}), \\ \frac{\delta v_{\mathbf{k}}}{\delta \text{Re}[\mathcal{B}_i(\mathbf{r})]} &= 2 \text{Re}[\mathcal{B}_i(\mathbf{r})] |\Psi_{0,\mathbf{k}}^{(-)}(\mathbf{r})|^2, \\ \frac{\delta v_{\mathbf{k}}}{\delta \text{Im}[\mathcal{B}_i(\mathbf{r})]} &= 2 \text{Im}[\mathcal{B}_i(\mathbf{r})] |\Psi_{0,\mathbf{k}}^{(-)}(\mathbf{r})|^2.\end{aligned}\quad (\text{B3})$$

The gradients of \tilde{W} are then given by,

$$\begin{aligned}\frac{\delta \tilde{W}}{\delta \text{Re}[\mathcal{B}_i(\mathbf{r})]} &= \frac{1}{N} \sum_{\mathbf{k}} \frac{1}{v_{\mathbf{k}}^2} \left[\frac{\delta |u_{\mathbf{k}}|^2}{\delta \text{Re}[\mathcal{B}_i(\mathbf{r})]} v_{\mathbf{k}} - |u_{\mathbf{k}}|^2 \frac{\delta v_{\mathbf{k}}}{\delta \text{Re}[\mathcal{B}_i(\mathbf{r})]} \right], \\ \frac{\delta \tilde{W}}{\delta \text{Im}[\mathcal{B}_i(\mathbf{r})]} &= \frac{1}{N} \sum_{\mathbf{k}} \frac{1}{v_{\mathbf{k}}^2} \left[\frac{\delta |u_{\mathbf{k}}|^2}{\delta \text{Im}[\mathcal{B}_i(\mathbf{r})]} v_{\mathbf{k}} - |u_{\mathbf{k}}|^2 \frac{\delta v_{\mathbf{k}}}{\delta \text{Im}[\mathcal{B}_i(\mathbf{r})]} \right].\end{aligned}\quad (\text{B4})$$

In our variational method, we set the parameter $\xi = 0.5$ and iterate until the difference in \tilde{W} between two consecutive steps is less than 10^{-8} .

-
- [1] E. Tang, J.-W. Mei, and X.-G. Wen, High-temperature fractional quantum Hall states, *Phys. Rev. Lett.* **106**, 236802 (2011).
[2] K. Sun, Z. Gu, H. Katsura, and S. Das Sarma, Nearly flatbands with nontrivial topology, *Phys. Rev. Lett.* **106**,

- 236803 (2011).
[3] T. Neupert, L. Santos, C. Chamon, and C. Mudry, Fractional quantum Hall states at zero magnetic field, *Phys. Rev. Lett.* **106**, 236804 (2011).
[4] N. Regnault and B. A. Bernevig, Fractional Chern insu-

- lator, *Phys. Rev. X* **1**, 021014 (2011).
- [5] D. N. Sheng, Z.-C. Gu, K. Sun, and L. Sheng, Fractional quantum hall effect in the absence of landau levels, *Nature Communications* **2**, 389 (2011).
 - [6] E. M. Spanton, A. A. Zibrov, H. Zhou, T. Taniguchi, K. Watanabe, M. P. Zaletel, and A. F. Young, Observation of fractional Chern insulators in a van der Waals heterostructure, *Science* **360**, 62 (2018).
 - [7] Y. Xie, A. T. Pierce, J. M. Park, D. E. Parker, E. Khalaf, P. Ledwith, Y. Cao, S. H. Lee, S. Chen, P. R. Forrester, K. Watanabe, T. Taniguchi, A. Vishwanath, P. Jarillo-Herrero, and A. Yacoby, Fractional Chern insulators in magic-angle twisted bilayer graphene, *Nature* **600**, 439 (2021).
 - [8] J. Cai, E. Anderson, C. Wang, X. Zhang, X. Liu, W. Holtzmann, Y. Zhang, F. Fan, T. Taniguchi, K. Watanabe, Y. Ran, T. Cao, L. Fu, D. Xiao, W. Yao, and X. Xu, Signatures of fractional quantum anomalous Hall states in twisted MoTe₂, *Nature* **622**, 63 (2023).
 - [9] Y. Zeng, Z. Xia, K. Kang, J. Zhu, P. Knüppel, C. Vaswani, K. Watanabe, T. Taniguchi, K. F. Mak, and J. Shan, Thermodynamic evidence of fractional Chern insulator in moiré MoTe₂, *Nature* **622**, 69 (2023).
 - [10] H. Park, J. Cai, E. Anderson, Y. Zhang, J. Zhu, X. Liu, C. Wang, W. Holtzmann, C. Hu, Z. Liu, T. Taniguchi, K. Watanabe, J.-H. Chu, T. Cao, L. Fu, W. Yao, C.-Z. Chang, D. Cobden, D. Xiao, and X. Xu, Observation of fractionally quantized anomalous Hall effect, *Nature* **622**, 74 (2023).
 - [11] F. Xu, Z. Sun, T. Jia, C. Liu, C. Xu, C. Li, Y. Gu, K. Watanabe, T. Taniguchi, B. Tong, J. Jia, Z. Shi, S. Jiang, Y. Zhang, X. Liu, and T. Li, Observation of integer and fractional quantum anomalous Hall effects in twisted bilayer MoTe₂, *Phys. Rev. X* **13**, 031037 (2023).
 - [12] Z. Lu, T. Han, Y. Yao, A. P. Reddy, J. Yang, J. Seo, K. Watanabe, T. Taniguchi, L. Fu, and L. Ju, Fractional quantum anomalous Hall effect in multilayer graphene, *Nature* **626**, 759 (2024).
 - [13] Z. Ji, H. Park, M. E. Barber, C. Hu, K. Watanabe, T. Taniguchi, J.-H. Chu, X. Xu, and Z.-X. Shen, Local probe of bulk and edge states in a fractional Chern insulator, *arXiv:2404.07157*.
 - [14] E. Redekop, C. Zhang, H. Park, J. Cai, E. Anderson, O. Sheekey, T. Arp, G. Babikyan, S. Salters, K. Watanabe, T. Taniguchi, X. Xu, and A. F. Young, Direct magnetic imaging of fractional Chern insulators in twisted MoTe₂ with a superconducting sensor, *arXiv:2405.10269*.
 - [15] K. Kang, B. Shen, Y. Qiu, Y. Zeng, Z. Xia, K. Watanabe, T. Taniguchi, J. Shan, and K. F. Mak, Evidence of the fractional quantum spin Hall effect in moiré MoTe₂, *Nature* **628**, 522 (2024).
 - [16] F. Wu, T. Lovorn, E. Tutuc, I. Martin, and A. H. MacDonald, Topological insulators in twisted transition metal dichalcogenide homobilayers, *Phys. Rev. Lett.* **122**, 086402 (2019).
 - [17] H. Yu, M. Chen, and W. Yao, Giant magnetic field from moiré induced Berry phase in homobilayer semiconductors, *National Science Review* **7**, 12 (2019).
 - [18] T. Devakul, V. Crépel, Y. Zhang, and L. Fu, Magic in twisted transition metal dichalcogenide bilayers, *Nature Communications* **12**, 6730 (2021).
 - [19] H. Li, U. Kumar, K. Sun, and S.-Z. Lin, Spontaneous fractional Chern insulators in transition metal dichalcogenide moiré superlattices, *Phys. Rev. Res.* **3**, L032070 (2021).
 - [20] V. Crépel and L. Fu, Anomalous Hall metal and fractional Chern insulator in twisted transition metal dichalcogenides, *Phys. Rev. B* **107**, L201109 (2023).
 - [21] N. Morales-Durán, J. Wang, G. R. Schleder, M. Angeli, Z. Zhu, E. Kaxiras, C. Repellin, and J. Cano, Pressure-enhanced fractional Chern insulators along a magic line in moiré transition metal dichalcogenides, *Phys. Rev. Res.* **5**, L032022 (2023).
 - [22] H. Goldman, A. P. Reddy, N. Paul, and L. Fu, Zero-field composite Fermi liquid in twisted semiconductor bilayers, *Phys. Rev. Lett.* **131**, 136501 (2023).
 - [23] J. Dong, J. Wang, P. J. Ledwith, A. Vishwanath, and D. E. Parker, Composite fermi liquid at zero magnetic field in twisted MoTe₂, *Phys. Rev. Lett.* **131**, 136502 (2023).
 - [24] A. P. Reddy and L. Fu, Toward a global phase diagram of the fractional quantum anomalous Hall effect, *Phys. Rev. B* **108**, 245159 (2023).
 - [25] A. P. Reddy, F. Alsallom, Y. Zhang, T. Devakul, and L. Fu, Fractional quantum anomalous Hall states in twisted bilayer MoTe₂ and WSe₂, *Phys. Rev. B* **108**, 085117 (2023).
 - [26] C. Wang, X.-W. Zhang, X. Liu, Y. He, X. Xu, Y. Ran, T. Cao, and D. Xiao, Fractional Chern insulator in twisted bilayer MoTe₂, *Phys. Rev. Lett.* **132**, 036501 (2024).
 - [27] C. Xu, J. Li, Y. Xu, Z. Bi, and Y. Zhang, Maximally localized Wannier functions, interaction models, and fractional quantum anomalous Hall effect in twisted bilayer MoTe₂, *Proceedings of the National Academy of Sciences* **121**, e2316749121 (2024).
 - [28] N. Mao, C. Xu, J. Li, T. Bao, P. Liu, Y. Xu, C. Felser, L. Fu, and Y. Zhang, Lattice relaxation, electronic structure and continuum model for twisted bilayer MoTe₂, *arXiv:2311.07533*.
 - [29] X.-W. Zhang, C. Wang, X. Liu, Y. Fan, T. Cao, and D. Xiao, Polarization-driven band topology evolution in twisted MoTe₂ and WSe₂, *Nature Communications* **15**, 4223 (2024).
 - [30] Y. Jia, J. Yu, J. Liu, J. Herzog-Arbeitman, Z. Qi, H. Pi, N. Regnault, H. Weng, B. A. Bernevig, and Q. Wu, Moiré fractional Chern insulators. i. first-principles calculations and continuum models of twisted bilayer MoTe₂, *Phys. Rev. B* **109**, 205121 (2024).
 - [31] W.-X. Qiu, B. Li, X.-J. Luo, and F. Wu, Interaction-driven topological phase diagram of twisted bilayer MoTe₂, *Phys. Rev. X* **13**, 041026 (2023).
 - [32] B. Li, W.-X. Qiu, and F. Wu, Electrically tuned topology and magnetism in twisted bilayer MoTe₂ at $\nu_h = 1$, *Phys. Rev. B* **109**, L041106 (2024).
 - [33] X.-J. Luo, W.-X. Qiu, and F. Wu, Majorana zero modes in twisted transition metal dichalcogenide homobilayers, *Phys. Rev. B* **109**, L041103 (2024).
 - [34] J. Yu, J. Herzog-Arbeitman, M. Wang, O. Vafek, B. A. Bernevig, and N. Regnault, Fractional Chern insulators versus nonmagnetic states in twisted bilayer MoTe₂, *Phys. Rev. B* **109**, 045147 (2024).
 - [35] A. Abouelkomsan, A. P. Reddy, L. Fu, and E. J. Bergholtz, Band mixing in the quantum anomalous Hall regime of twisted semiconductor bilayers, *Phys. Rev. B* **109**, L121107 (2024).
 - [36] X.-Y. Song, Y.-H. Zhang, and T. Senthil, Phase transitions out of quantum Hall states in moiré materials, *Phys.*

- Rev. B **109**, 085143 (2024).
- [37] F.-R. Fan, C. Xiao, and W. Yao, Orbital Chern insulator at $\nu = -2$ in twisted MoTe₂, *Phys. Rev. B* **109**, L041403 (2024).
 - [38] X. Liu, Y. He, C. Wang, X.-W. Zhang, T. Cao, and D. Xiao, Gate-tunable antiferromagnetic Chern insulator in twisted bilayer transition metal dichalcogenides, *Phys. Rev. Lett.* **132**, 146401 (2024).
 - [39] N. Morales-Durán, N. Wei, J. Shi, and A. H. MacDonald, Magic angles and fractional Chern insulators in twisted homobilayer transition metal dichalcogenides, *Phys. Rev. Lett.* **132**, 096602 (2024).
 - [40] J. Shi, N. Morales-Durán, E. Khalaf, and A. H. MacDonald, Adiabatic approximation and Aharonov-Casher bands in twisted homobilayer TMDs, [arXiv:2404.13455](#).
 - [41] V. Crépel, N. Regnault, and R. Queiroz, Chiral limit and origin of topological flat bands in twisted transition metal dichalcogenide homobilayers, *Communications Physics* **7**, 146 (2024).
 - [42] T. Wang, M. Wang, W. Kim, S. G. Louie, L. Fu, and M. P. Zaletel, Topology, magnetism and charge order in twisted MoTe₂ at higher integer hole fillings, [arXiv:2312.12531](#).
 - [43] A. P. Reddy, N. Paul, A. Abouelkomsan, and L. Fu, Non-abelian fractionalization in topological minibands, [arXiv:2403.00059](#).
 - [44] C. Xu, N. Mao, T. Zeng, and Y. Zhang, Multiple Chern bands in twisted MoTe₂ and possible non-abelian states, [arXiv:2403.17003](#).
 - [45] C.-E. Ahn, W. Lee, K. Yananose, Y. Kim, and G. Y. Cho, First Landau level physics in second Moiré band of 2.1° twisted bilayer MoTe₂, [arXiv:2403.19155](#).
 - [46] C. Wang, X.-W. Zhang, X. Liu, J. Wang, T. Cao, and D. Xiao, Higher Landau-level analogues and signatures of non-abelian states in twisted bilayer MoTe₂, [arXiv:2404.05697](#).
 - [47] Y.-H. Zhang, Non-abelian and abelian descendants of vortex spin liquid: fractional quantum spin Hall effect in twisted MoTe₂, [arXiv:2403.12126](#).
 - [48] C.-M. Jian, M. Cheng, and C. Xu, Minimal fractional topological insulator in half-filled conjugate moiré Chern bands, [arXiv:2403.07054](#).
 - [49] I. S. Villadiego, Halperin states of particles and holes in ideal time reversal invariant pairs of Chern bands and the fractional quantum spin Hall effect in Moiré MoTe₂, [arXiv:2403.12185](#).
 - [50] J. May-Mann, A. Stern, and T. Devakul, Theory of half-integer fractional quantum spin Hall insulator edges, [arXiv:2403.03964](#).
 - [51] M. Wang, X. Wang, and O. Vafek, Interacting phase diagram of twisted bilayer MoTe₂ in magnetic field, [arXiv:2405.14811](#).
 - [52] S. Das Sarma and M. Xie, On the zero-field quantization of the anomalous quantum Hall effect in two-dimensional moiré layers, *Phys. Rev. B* **109**, L121104 (2024).
 - [53] X.-L. Qi, Generic wave-function description of fractional quantum anomalous Hall states and fractional topological insulators, *Phys. Rev. Lett.* **107**, 126803 (2011).
 - [54] Y.-L. Wu, N. Regnault, and B. A. Bernevig, Gauge-fixed Wannier wave functions for fractional topological insulators, *Phys. Rev. B* **86**, 085129 (2012).
 - [55] S. A. Parameswaran, R. Roy, and S. L. Sondhi, Fractional quantum Hall physics in topological flat bands, *Comptes Rendus. Physique* **14**, 816 (2013).
 - [56] T. S. Jackson, G. Möller, and R. Roy, Geometric stability of topological lattice phases, *Nature Communications* **6**, 8629 (2015).
 - [57] M. Claassen, C. H. Lee, R. Thomale, X.-L. Qi, and T. P. Devereaux, Position-momentum duality and fractional quantum Hall effect in chern insulators, *Phys. Rev. Lett.* **114**, 236802 (2015).
 - [58] G. Tarnopolsky, A. J. Kruchkov, and A. Vishwanath, Origin of magic angles in twisted bilayer graphene, *Phys. Rev. Lett.* **122**, 106405 (2019).
 - [59] P. J. Ledwith, G. Tarnopolsky, E. Khalaf, and A. Vishwanath, Fractional Chern insulator states in twisted bilayer graphene: An analytical approach, *Phys. Rev. Res.* **2**, 023237 (2020).
 - [60] J. Wang, Y. Zheng, A. J. Millis, and J. Cano, Chiral approximation to twisted bilayer graphene: Exact intravalley inversion symmetry, nodal structure, and implications for higher magic angles, *Phys. Rev. Res.* **3**, 023155 (2021).
 - [61] J. Wang, J. Cano, A. J. Millis, Z. Liu, and B. Yang, Exact Landau level description of geometry and interaction in a flatband, *Phys. Rev. Lett.* **127**, 246403 (2021).
 - [62] T. Ozawa and B. Mera, Relations between topology and the quantum metric for Chern insulators, *Phys. Rev. B* **104**, 045103 (2021).
 - [63] B. Mera and T. Ozawa, Kähler geometry and Chern insulators: Relations between topology and the quantum metric, *Phys. Rev. B* **104**, 045104 (2021).
 - [64] J. Wang and Z. Liu, Hierarchy of ideal flatbands in chiral twisted multilayer graphene models, *Phys. Rev. Lett.* **128**, 176403 (2022).
 - [65] P. J. Ledwith, A. Vishwanath, and E. Khalaf, Family of ideal Chern flatbands with arbitrary Chern number in chiral twisted graphene multilayers, *Phys. Rev. Lett.* **128**, 176404 (2022).
 - [66] P. J. Ledwith, A. Vishwanath, and D. E. Parker, Vortexability: A unifying criterion for ideal fractional Chern insulators, *Phys. Rev. B* **108**, 205144 (2023).
 - [67] J. Wang, S. Klevtsov, and Z. Liu, Origin of model fractional Chern insulators in all topological ideal flatbands: Explicit color-entangled wave function and exact density algebra, *Phys. Rev. Res.* **5**, 023167 (2023).
 - [68] J. Dong, P. J. Ledwith, E. Khalaf, J. Y. Lee, and A. Vishwanath, Many-body ground states from decomposition of ideal higher Chern bands: Applications to chirally twisted graphene multilayers, *Phys. Rev. Res.* **5**, 023166 (2023).
 - [69] M. Fujimoto, D. E. Parker, J. Dong, E. Khalaf, A. Vishwanath, and P. Ledwith, Higher vortexability: zero field realization of higher Landau levels, [arXiv:2403.00856](#).
 - [70] T. Tan, A. P. Reddy, L. Fu, and T. Devakul, Designing topology and fractionalization in narrow gap semiconductor films via electrostatic engineering, [arXiv:2402.03085](#).
 - [71] N. Nagaosa and Y. Tokura, Topological properties and dynamics of magnetic skyrmions, *Nature Nanotechnology* **8**, 899 (2013).
 - [72] R. B. Laughlin, Anomalous quantum Hall effect: An incompressible quantum fluid with fractionally charged excitations, *Phys. Rev. Lett.* **50**, 1395 (1983).
 - [73] Z. Liu, B. Mera, M. Fujimoto, T. Ozawa, and J. Wang, Theory of generalized Landau levels and implication for non-abelian states, [arXiv:2405.14479](#).
 - [74] S. Ghorashi, A. Dunbrack, A. Abouelkomsan, J. Sun, X. Du, and J. Cano, Topological and stacked flat bands in bilayer graphene with a superlattice potential, *Phys.*

- [Rev. Lett. **130**, 196201 \(2023\)](#).
- [75] X. Wan, S. Sarkar, S.-Z. Lin, and K. Sun, Topological exact flat bands in two-dimensional materials under periodic strain, [Phys. Rev. Lett. **130**, 216401 \(2023\)](#).
- [76] Q. Gao, J. Dong, P. Ledwith, D. Parker, and E. Khalaf, Untwisting moiré physics: Almost ideal bands and fractional Chern insulators in periodically strained monolayer graphene, [Phys. Rev. Lett. **131**, 096401 \(2023\)](#).
- [77] F. D. M. Haldane, A modular-invariant modified Weierstrass sigma-function as a building block for lowest-Landau-level wavefunctions on the torus, [Journal of Mathematical Physics **59**, 071901 \(2018\)](#).